



Full Length Article

Trivalent lanthanum and ytterbium doped *meso*-silica/ceria abrasive systems toward chemical mechanical polishing (CMP) and ultraviolet irradiation-assisted photochemical mechanical polishing (PCMP)

Zihan Kou^a, Chao Wang^{b,*}, Wenjin Zhou^a, Ailian Chen^c, Yang Chen^{a,*}^a School of Materials Science and Engineering, Changzhou University, Changzhou, Jiangsu 213164, PR China^b Institute of Machinery Manufacturing Technology, China Academy of Engineering Physics (CAEP), Mianyang, Sichuan 621900, PR China^c School of Mechanical Engineering and Rail Transit, Changzhou University, Changzhou, Jiangsu 213164, PR China

ARTICLE INFO

ABSTRACT

Keywords:

CeO₂
Doping
Mesoporous silica
Abrasive system
Polishing
Ultraviolet-irradiation assistance

Ceria (CeO₂)-based abrasives are widely utilized in ultra-precision grinding and chemical mechanical polishing (CMP) applications over silica materials due to their unique physicochemical properties. Both mechanical and chemical contributions to polishing processes are highly affected by the size, shape, structure, component, defect of CeO₂ abrasives. Herein, the composites involved mesoporous silica (mSiO₂) cores and La- or Yb-doped CeO₂ shells were synthesized and characterized in terms of X-ray diffractometry, scanning electron microscopy, transmission electron microscopy, Raman spectroscopy, scanning transmission electron microscopy-energy dispersive X-ray mapping methods. The polishing effectiveness of the proposed composites toward quartz glass was experimentally evaluated under both CMP and ultraviolet irradiation-assisted photochemical mechanical polishing (PCMP) conditions. The polishing results indicated that the low-modulus mSiO₂ cores strongly exerted the cushion effects for the friction and abrasion to substrates. Consequently, the heterostructured mSiO₂/La-CeO₂ and mSiO₂/Yb-CeO₂ abrasive systems offered nearly non-damage and ultra-smooth surfaces with angstrom-level roughness compared to conventional rigid abrasives. The enriched Ce³⁺ and oxygen vacancy defects at La- and Yb- doped CeO₂ surfaces were responsible for the improvements of tribochemical and photochemical activities, thus allowing evidently enhanced removal efficiency with the assistance of ultraviolet irradiation. A possible polishing mechanism on the multi-component abrasive systems was also proposed.

1. Introduction

Chemical mechanical polishing/planarization (CMP) [1–5] has emerged as an available and powerful technique for globally or locally smoothing and planarizing metals, ceramics, and polymers with surface roughness of sub-nanometer scale. CMP can be regarded as a complex chemical etching process (surface modification) and free abrasive polishing (material removal). Typically, these processes aim to minimize or even eliminate the surface and subsurface damage typically involved in mechanical abrasion and surface corrosion generated by etching. Nevertheless, it is still a challenge to achieving both further high removal rate and high surface quality.

Complex polishing methods and systems pose both challenges and opportunities in comparison to the conventional CMP technique. Up to now, advanced oxidation process (ozone, photocatalysis, photo-Fenton,

electro-Fenton, Fenton-like, etc.), physical field and external energy (plasma, laser, ultraviolet radiation, thermal, ultrasonic, magnetic, electromagnetic, magnetorheological, electrochemical, photochemical, etc.) [6–12] have been introduced into traditional CMP processes for further improved performance. Among these new polishing techniques, ultraviolet irradiation-assisted photochemical mechanical polishing (PCMP) [13–24] has attracted growing interest in recent years and deserve more attention in system optimization, because it can be easily to be performed by installing a peripheral light source with a conventional polishing equipment. In the case of PCMP, highly reactive oxygen species (typically hydroxyl radicals) can be effectively produced in polishing slurries via photocatalysis and/or photo-Fenton reactions, thus softening the hard surface of substrate materials and accelerating the removal of the modified surface layers.

Polishing slurries commonly consist of liquid phase and solid phase,

* Corresponding authors.

E-mail addresses: wangchaohit@126.com (C. Wang), cy.jpu@126.com (Y. Chen).

except for some abrasive-free slurries. Liquid phase typically involves deionized water, oxidizers, dispersants, pH regulators, stabilizers, and other surfactants. Solid phase typically contains non-metallic oxides served as abrasive particles, for example, silica (SiO_2), ceria (CeO_2), alumina (Al_2O_3), iron oxide (Fe_2O_3), tin oxide (SnO_2), tungsten oxide (WO_3), zirconia (ZrO_2), yttria (Y_2O_3), etc. Of these oxides, CeO_2 is the most efficient abrasives in polishing slurries for processing silica-involved materials due to its high tribocatalytic activity and removal efficiency.

Abrasive particles in polishing slurries are essential for CMP performance, even though their actual role is not entirely clear. It is commonly recognized that the size, composition, shape, hardness, modulus, and surface chemistry of abrasive particles are also thought to play a key role in CMP practices. Nevertheless, the most popular oxide abrasives still remain some challenges, for example, surface damage, surface roughness, removal selectivity, removal efficiency, etc. Fortunately, some of these shortcomings associated with the use of conventional abrasives can be effectively controlled by the introduction of novel abrasive systems. In the past decade, tremendous efforts have been made towards the development of mixed, modified, porous, non-spherical, and composite abrasives with well-designed size, morphology, structure as well as proper constituent and/or composition. Great progress has been achieved in developing CeO_2 -coated polymer [6,16–18,26–28], solid or mesoporous SiO_2 [19,20,29], carbon [17], h-BN [30] abrasive systems, due to their excellent properties such as rich surface defect, controlled porosity, low overall modulus, good dispersion stability, etc. Core/shell heterostructures [31,32] with tunable compositions are attracting great interest because they can have functionalities in both the cores and the shells, making these materials applicable in advanced polishing practices. Nevertheless, there are still few reports focused on the PCMP practices over optical quartz glasses using CeO_2 -involved core/shell abrasive systems.

In this work, lanthanum (La)- or ytterbium (Yb)-doped CeO_2 nanocrystals were deposited on mesoporous silica (m SiO_2) nanospheres using a facile *in-situ* chemical synthesis. The experimental evidences of defect evolution (typically Ce^{3+} and oxygen vacancy) in La- and Yb-doped CeO_2 were explored via Raman spectroscopy, X-ray diffractometry, X-ray photoelectron spectrometer, and high angle annular dark field (HAADF) imaging operated in scanning transmission electron microscope (STEM) mode. The resulting m SiO_2 /La- CeO_2 and m SiO_2 /Yb- CeO_2 composites were utilized as novel core/shell abrasive systems for improved polishing performance toward optical quartz glasses. The large m SiO_2 core aim to serve as a low-modulus carrier for the CeO_2 nanoparticles and brings them in contact with the substrates more gently and efficiently during polishing. Doping trivalent La or Yb ions in CeO_2 lattice structures are expected to create more surface defects such as Ce^{3+} and oxygen vacancies (VOs) [33], thus leading to the enhancement of tribocatalytic and photochemical activities. The superiority of the proposed abrasive systems was verified by comparing surface quality and removal rate with non-porous rigid CeO_2 -based abrasives under both CMP and ultraviolet irradiation-assisted PCMP. Furthermore, a possible polishing mechanism was discussed in terms of interfacial abrasive–substrate contact, photochemical surface modification, and tribocatalytic material removal.

2. Experimental section

2.1. Materials and reagents

All chemicals used were obtained from Shanghai Chemical Reagent Co., Ltd. (China), including cerium nitrate hexahydrate ($\text{Ce}(\text{NO}_3)_3 \cdot 6\text{H}_2\text{O}$, AR), lanthanum nitrate hexahydrate ($\text{La}(\text{NO}_3)_3 \cdot 6\text{H}_2\text{O}$, AR), yttrium nitrate hexahydrate ($\text{Yb}(\text{NO}_3)_3 \cdot 6\text{H}_2\text{O}$, AR), ethanol ($\text{C}_2\text{H}_5\text{OH}$, AR), acetone ($\text{C}_3\text{H}_6\text{O}$, AR), hexamethylenetetramine ($\text{C}_6\text{H}_{12}\text{N}_4$, CP), hydrogen peroxide (H_2O_2 , 30 wt%, AR), sodium hydroxide (NaOH , AR), cetyltrimethylammonium bromide (CTAB, AR), sodium dodecyl

sulfate (SDS, AR), and tetraethyl orthosilicate (TEOS, AR). All chemicals were used as received without further purification.

2.2. Powder synthesis

All preparations were performed in an oil bath equipped with a temperature controller and a magnetic stirrer. In a typical synthesis procedure, spherical m SiO_2 particles (ca. 200 nm) were first prepared via a templated-assisted Stöber method involved the interfacial assembly of CTAB/TEOS in ethanol/water mixed system, as described in our previous work [34]. Briefly, 0.2 g of m SiO_2 was dispersed into the 47.4 g of ethanol with ultrasound for 30 min. After that, a mixture of 0.5 g of $\text{Ce}(\text{NO}_3)_3 \cdot 6\text{H}_2\text{O}$, 0.1 g of $\text{La}(\text{NO}_3)_3 \cdot 6\text{H}_2\text{O}$ (or $\text{Yb}(\text{NO}_3)_3 \cdot 6\text{H}_2\text{O}$), 0.96 g of $\text{C}_6\text{H}_{12}\text{N}_4$ (as a precipitant), and 40 g of deionized water was added to the above solution and stirred constantly for 30 min, respectively. Subsequently, the suspension was heated to 75 °C in an oil bath and maintained for 2 h under magnetic stirring (300 r/min). The resulting products were centrifuged, washed with deionized water and ethanol several times, and dried in an oven. Finally, the m SiO_2 /La- CeO_2 and m SiO_2 /Yb- CeO_2 samples were obtained by annealing the products in air at 650 °C for 2 h with a heating rate of 10 °C/min⁻¹. Herein, the Ce^{3+} and La^{3+} (or Yb^{3+}) cations were mixed at the stoichiometric molar ratio of 0.85: 0.15, i.e., the doping amounts in La- CeO_2 and Yb- CeO_2 nanocrystals were set at ca. 15 %. For comparison, the undoped m SiO_2 /Ce O_2 composites were also fabricated. In addition, the solid silica (s SiO_2)-involved non-porous s SiO_2 /Ce O_2 particles with comparable core size and shell thickness were prepared using a similar procedure mentioned above.

2.3. Powder characterization

Phase identification was performed via X-ray diffractometry (XRD) on a Rigaku D/Max 2500 PC diffractometer operated at 40 kV/120 mA using nickel-filtered Cu K α radiation (1.54056 Å) in the range of $2\theta = 20^\circ$ – 80° with a scanning speed of 10°/min and an acquisition step of 0.02° (2θ). Lattice parameters of the (La- and Yb-) doped CeO_2 were determined by fitting the observed reflections with a least-squares refinement program. Crystallite sizes were calculated by the X-ray line-broadening technique performed on the (111) diffraction using the Scherrer equation ($D = 0.9\lambda/\beta\cos\theta$), where D is the average crystallite size, λ is the wavelength of incident X-rays (1.54056 Å), β is the corrected half-width, and θ is the diffraction angle.

Particle morphology and agglomeration of the as-synthesized powders were characterized with a field-emission scanning electron microscope (FESEM, Model: SUPRA55, Zeiss). The powder samples were ultrasonically dispersed in ethanol, and the suspension was spread on the surface of a polished silicon wafer. After drying in air, a thin layer of gold was coated on the sample surface for conductivity before observation. The particle size distributions of the samples were analyzed using image analysis software (Nano Measurer V1.2). Transmission electron microscopy (TEM) images and selected-area electron diffraction (SEAD) patterns were obtained by a JEOL JEM-2100 high-resolution (HR) TEM apparatus. Energy dispersive spectroscopy (EDS) analysis was conducted with an equipped Oxford EDS detector. A FEI Talos 200 s microscope (equipped with an energy dispersive X-ray (EDX) detector) with a high-angle annular dark field (HAADF) function was used for acquiring elemental maps. All samples dispersing in aqueous solution were deposited a single drop on copper grids for TEM observations. Raman spectroscopy analyses were performed on a DXR Raman spectrometer (ThermoFisher, UK) with an excitation laser wavelength of 532 nm in the range of 200–800 cm⁻¹. Zeta potential measurements were carried out on a Nano-ZS Zetasizer (Malvern, UK). The surface composition and oxidation state the samples were analyzed using a ULVAC-Phi PHI-5000 VP III X-ray photoelectron spectrometer (XPS) with Al K α X-ray source ($h\nu = 1486.6$ eV). And the C 1 s reference at 284.8 eV was used for the binding energy calibration.

2.4. Polishing experiments

The BK7 (K9) optical quartz glasses with a dimension of $20.0 \times 20.0 \times 2.0$ mm was obtained from Kejing Materials Technology Co., Ltd. (Hefei, China), and utilized as substrates in all polishing tests. The surface morphology analysis of the as-received workpiece was performed using an atomic force microscope (AFM), revealing a rough appearance (Fig. 1) with an average surface roughness (R_a) of ca. 111 nm and a root-mean-square roughness (R_q) of ca. 137 nm. The corresponding profile curves show the maximum peak-to-valley (PV) value of ca. 344 nm. In this work, the sample quartz glasses underwent rough grinding/polishing and precision polishing procedures using a benchtop polisher (TegraForce-1/TrgraPol-15, Struers A/S, Denmark). In the rough polishing stage, the as-received quartz glasses were mechanically pre-finished using commercial calcined CeO_2 abrasives with mixed particle sizes ranged from 100 nm to 1000 nm (obtained from Changzhou Geoquin Nano New Material Co., Ltd.), which provided samples with reduced surface roughness for subsequent precision polishing processes. After 60-min rough polishing, the surface roughness of the quartz glass significantly reduced, as determined by a 3D noncontact interferometric microscope and an atomic force microscope.

Precision polishing tests were performed on a benchtop TegraForce-1/TrgraPol-15 polisher coupled with a MD-Chem porous polyurethane polishing pad (Struers A/S) and a 250-W halogen lamp (ultraviolet light source) with a wavelength of 365 nm for PCMP experiments. The schematic view of the ultraviolet irradiation-assisted PCMP apparatus was described in Fig. 2. The polishing was performed at a downforce of 3.0 psi with a coupon area of 20.0×20.0 mm 2 and a polishing time of 30 min. The head/platen rotational speed was 120/90 rpm, and the slurry flow rate was 50 mL/min for all the experiments.

Polishing slurries were prepared with the $\text{mSiO}_2/\text{La-CeO}_2$, $\text{mSiO}_2/\text{Yb-CeO}_2$, or $\text{sSiO}_2/\text{CeO}_2$ composite abrasives at a concentration of 1.0 wt% in deionized water. These slurries were then modified through pH adjustment (8.0–8.5) and the addition of oxidant (H_2O_2 , 1.0 wt%) and surfactant (SDS, 0.5 wt%). The dispersant aimed to enhance the dispensability of the abrasives in polishing slurries. The polishing slurries were irradiated with ultraviolet light for 10 min prior to PCMP experiments.

The BK7 substrates before and after polishing were ultrasonically

cleaned with deionized water and acetone, and then dried and stored in nitrogen prior to analysis. Surface morphology, defect, and roughness were investigated through an atomic force microscope (AFM, Nanoman VS, formerly Digital Instruments & Veeco Instruments, equipped with a Dimension V controller) in tapping mode using a commercial Budget-Sensors Tap300Al-G silicon probe with a max tip radius of 10 nm. The scanning speed was 1.0 Hz, and the scanning areas with a resolution of 512 px \times 512 px were fixed at 5.0 $\mu\text{m} \times$ 5.0 μm . Five measurement positions from the edge to the center of every workpiece surface were randomly selected to ensure the credibility of the surface roughness determinations. The surface quality was evaluated in terms of PV, R_q , R_a , surface area difference (SAD), etc. Material removal rates (RRs) were calculated in terms of the equation (1):

$$RR = \Delta m / \rho s t (1)$$

Herein, Δm is the difference in the workpiece weight measured using a Mettler Toledo XS105 analytical balance (accuracy of 0.01 mg) before and after polishing, ρ is the density of quartz glasses (2.2 g/cm 3), s is the workpiece area of optical quartz glasses, t is the polishing time. The presented data (average surface roughness and RR, and its standard deviation) were calculated from three runs.

3. Results and discussion

3.1. Morphological, crystallographic and spectroscopic analyses

FESEM observations were utilized to examine the morphology and particle diameter change of mSiO_2 and $\text{mSiO}_2/\text{La-CeO}_2$ products. Prior to the synthesis of core/shell composites, monodispersed mSiO_2 spheres (Fig. 3a) were prepared as the core materials via a modified CTAB-assisted Stöber approach. After coating, the resulting $\text{mSiO}_2/\text{La-CeO}_2$ (Fig. 3c) still remains well-defined spherical shapes with rough appearances, clearly indicating the presence of the grafted La-CeO_2 nanoparticles. The particle-size distributions (Fig. 3b and d) of the samples were explored by Gauss fitting and counting 50 mSiO_2 and $\text{mSiO}_2/\text{La-CeO}_2$ spheres taken from FESEM images. Corresponding average diameter sizes of experimentally obtained mSiO_2 and $\text{mSiO}_2/\text{La-CeO}_2$ were determined to be 208.1 ± 24.9 and 227.7 ± 27.1 nm, respectively. Obtained from the differences between the mean sizes of

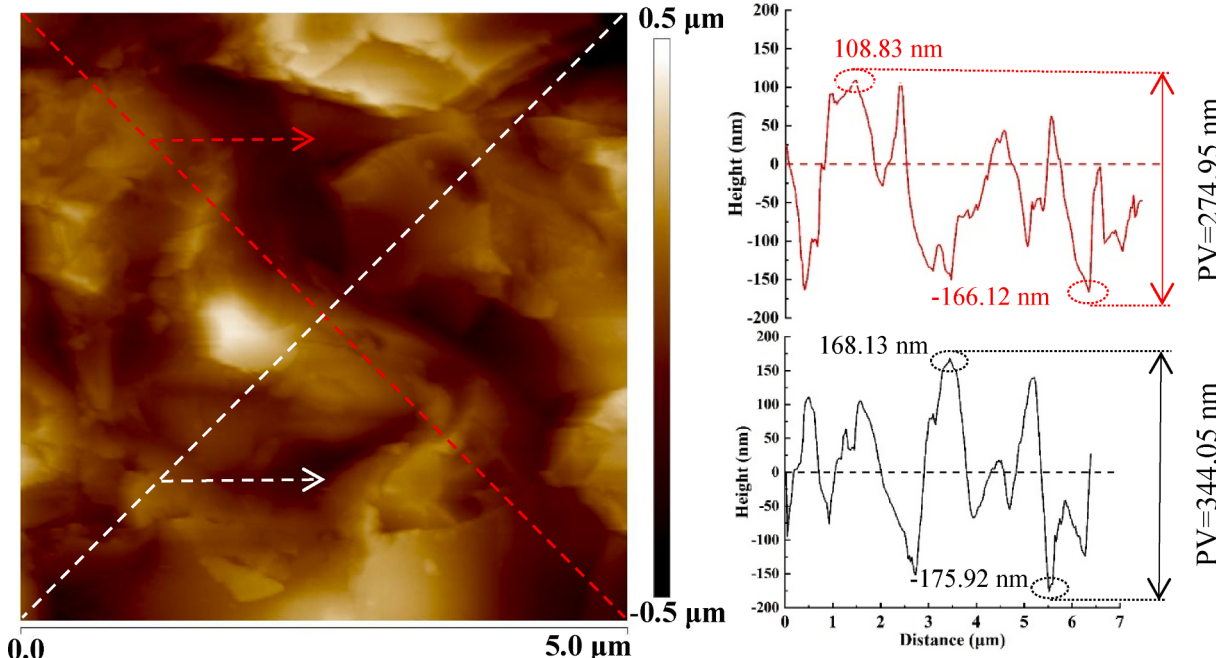


Fig. 1. Surface features the as-received BK7 (K9) quartz glass.

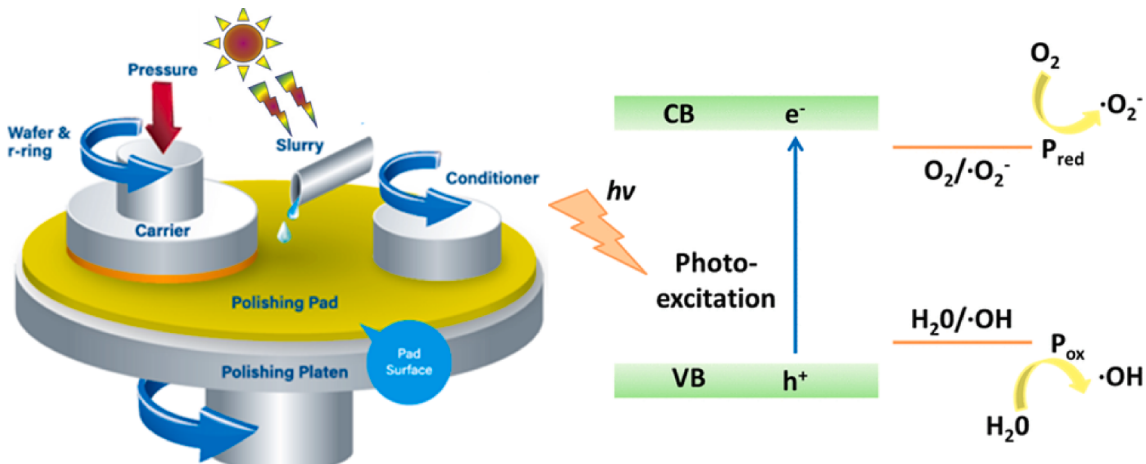


Fig. 2. Schematic of the ultraviolet irradiation-assisted PCMP polishing setup.

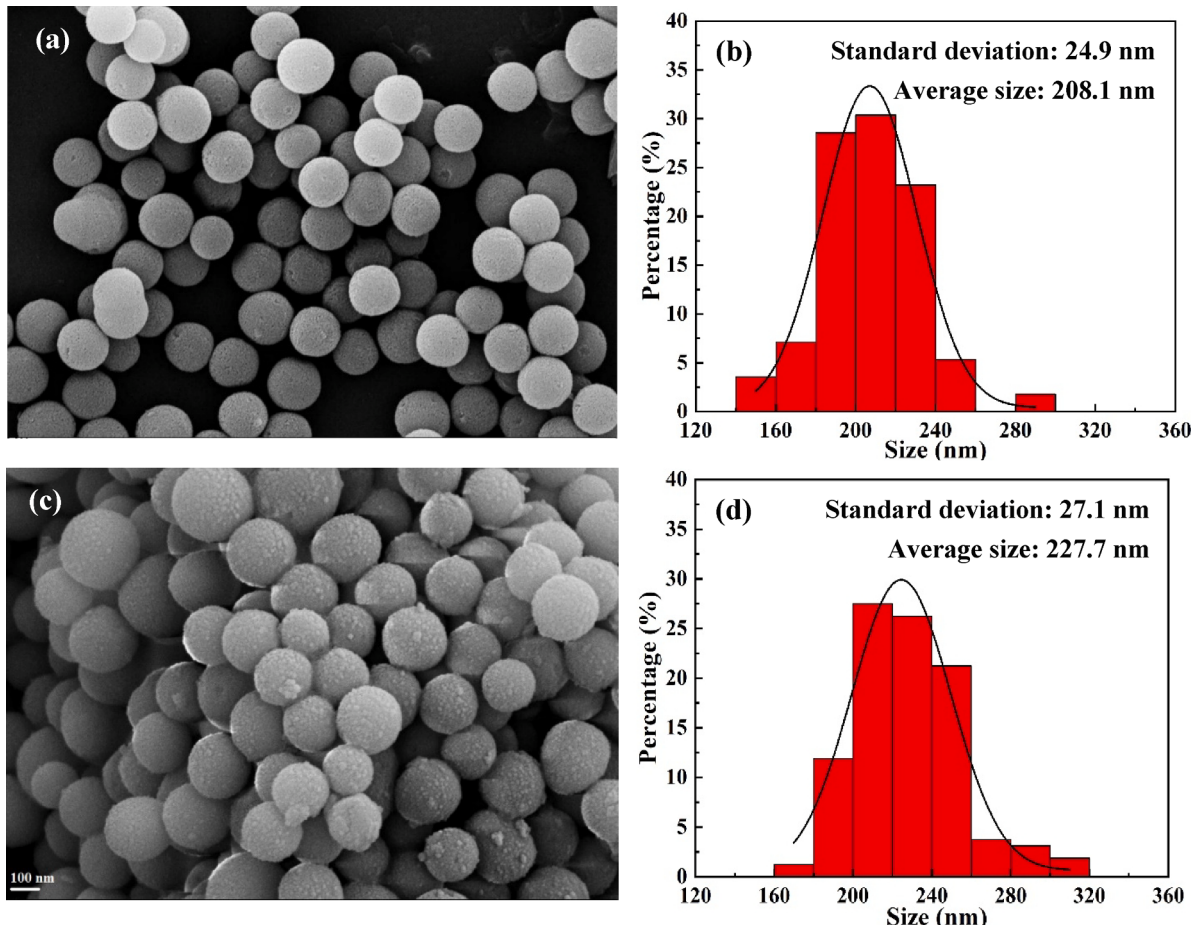


Fig. 3. FESEM images and the corresponding particle-size distributions of (a, c) mSiO₂ and (b, d) mSiO₂/La-CeO₂ samples.

mSiO₂ and mSiO₂/La-CeO₂ particles, the CeO₂ shell thicknesses were estimated to be about 10 nm.

TEM investigations were performed to further investigate the presence of CeO₂ nanocrystals on the surfaces of mSiO₂ cores. By comparison with the smooth bare mSiO₂ (Fig. 4a) with relative-low electron contrast, the low-magnification TEM image of mSiO₂/La-CeO₂ (Fig. 4b) reveals the formation of uniform spherical particles with rough appearances and relative-high electron contrast. The strawberry-like surfaces of mSiO₂ have a densely packed coverage of CeO₂ nanoparticles,

which agrees well with the FESEM results (Fig. 3). In addition, the CeO₂ nanoparticles involved in mSiO₂/La-CeO₂ and mSiO₂/Yb-CeO₂ composites are well-distributed on the shell surfaces and each consisted of many nanocrystals with a size range of approximately 2–5 nm, as confirmed by high-magnification TEM analyses (Fig. 4c and d). The representative HRTEM images (Fig. 4e and f) taken from the La- and Yb-doped CeO₂ depict the distinct lattice fringes of ca. 0.33 and 0.32 nm, corresponding to the spacing of the (1 1 1) planes of CeO₂. The crystalline nature of La-CeO₂ is also evidenced by the SAED pattern (Fig. 4g).

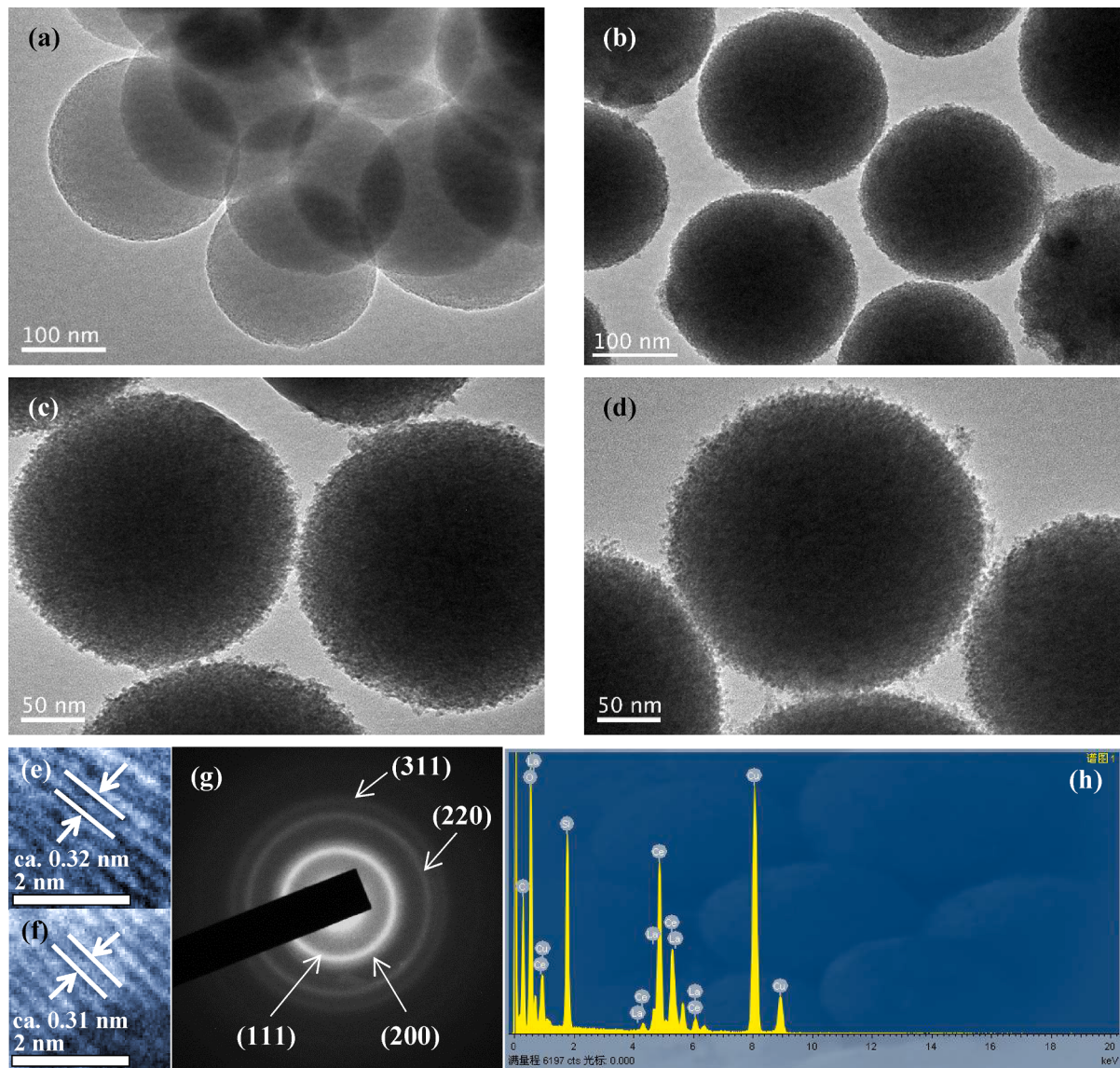


Fig. 4. Low- and high-magnification TEM, HRTEM images, SAED pattern, and EDS spectrum of (a) mSiO₂, (b, c, e, g, h) mSiO₂/La-CeO₂, (d, f) mSiO₂/Yb-CeO₂ samples.

There are four diffraction rings can be indexed to (111), (200), (220), and (311) crystal planes of CeO₂, further verifying the polycrystalline characteristics. EDS measurement was performed at several locations throughout the specimens, and a representative EDS spectrum on mSiO₂/La-CeO₂, as shown in Fig. 4h, demonstrated that cerium (Ce), lanthanum (La), silicon (Si), and oxygen (O) were electrodeposited. Result of the EDS analysis confirms that the existence of Ce, La, Si, and O elements, which are in accordance with the starting materials involved in material preparations.

The structure and elemental distribution of an individual mSiO₂/Yb-CeO₂ particle were characterized in terms of HAADF-STEM imaging in conjunction with EDX elemental mapping. Micrographs of mSiO₂/Yb-CeO₂ (Fig. 5 a) with element mapping reveal the existence and homogeneous distributions of O (Fig. 5b), Si (Fig. 5c), Ce (Fig. 5d), and Yb (Fig. 5e) in a single Yb-doped composite particle. Furthermore, the Si-Ce-Yb overlap (Fig. 5f) shows that the distribution of Si is mainly located in the core region, whereas Ce and Yb are observed to be located on the outer shells, confirming the successful construction of well-defined core/shell structures for mSiO₂/Yb-CeO₂ composites. The elemental content data of Ce, Yb, Si, O, etc. (Fig. 5g) show an approximate atom ratio of Ce to Yb is 6.66: 1, hence the Yb/(Ce + Yb) atomic

ratio is ca. 0.131 in the mSiO₂/Yb-CeO₂ samples.

XRD patterns were conducted to characterize the crystal structures of the pure, La- and Yb-doped mSiO₂/CeO₂ samples. As shown in Fig. 6, the typical XRD diffraction peaks at ca. 28.6°, 47.5°, 56.3°, and 77.4° can be ascribed to the (111), (220), (311), and (331) facets of *Fm3m* face-centered-cubic CeO₂ structure (JCPDS No. 43—1002). No other peaks of La₂O₃ or Yb₂O₃ can be found in the XRD patterns, which confirms that La³⁺ and Yb³⁺ ions are successfully doped into CeO₂ crystal lattices. In addition, the (111) plane diffractions of La- and Yb-doped samples slightly shift to lower diffracting angles, also revealing an expansion in the unit cell. These XRD results infer the doped species are highly dispersed in lattice site positions, indicating the formation of Ce-La-O or Ce-Yb-O solid solutions. The lattice parameters of pure, La- and Yb-doped CeO₂ nanocrystals were determined to be 5.405, 5.452, and 5.439 Å, respectively. The lattice parameters slightly increase with an increased ionic radius of the dopant, which are in well agreement with the previous experimental results [35–38]. The ionic radii of La³⁺ (1.16 Å) [39] and Yb³⁺ (0.99 Å) [39] cations are slightly larger than that of Ce⁴⁺ (0.97 Å) [39], therefore the partial substitution of Ce⁴⁺ by La³⁺ or Yb³⁺ cations will cause an expansion of the cubic CeO₂ lattices. Based on the Debye-Scherrer equation, the average crystallite sizes of CeO₂,

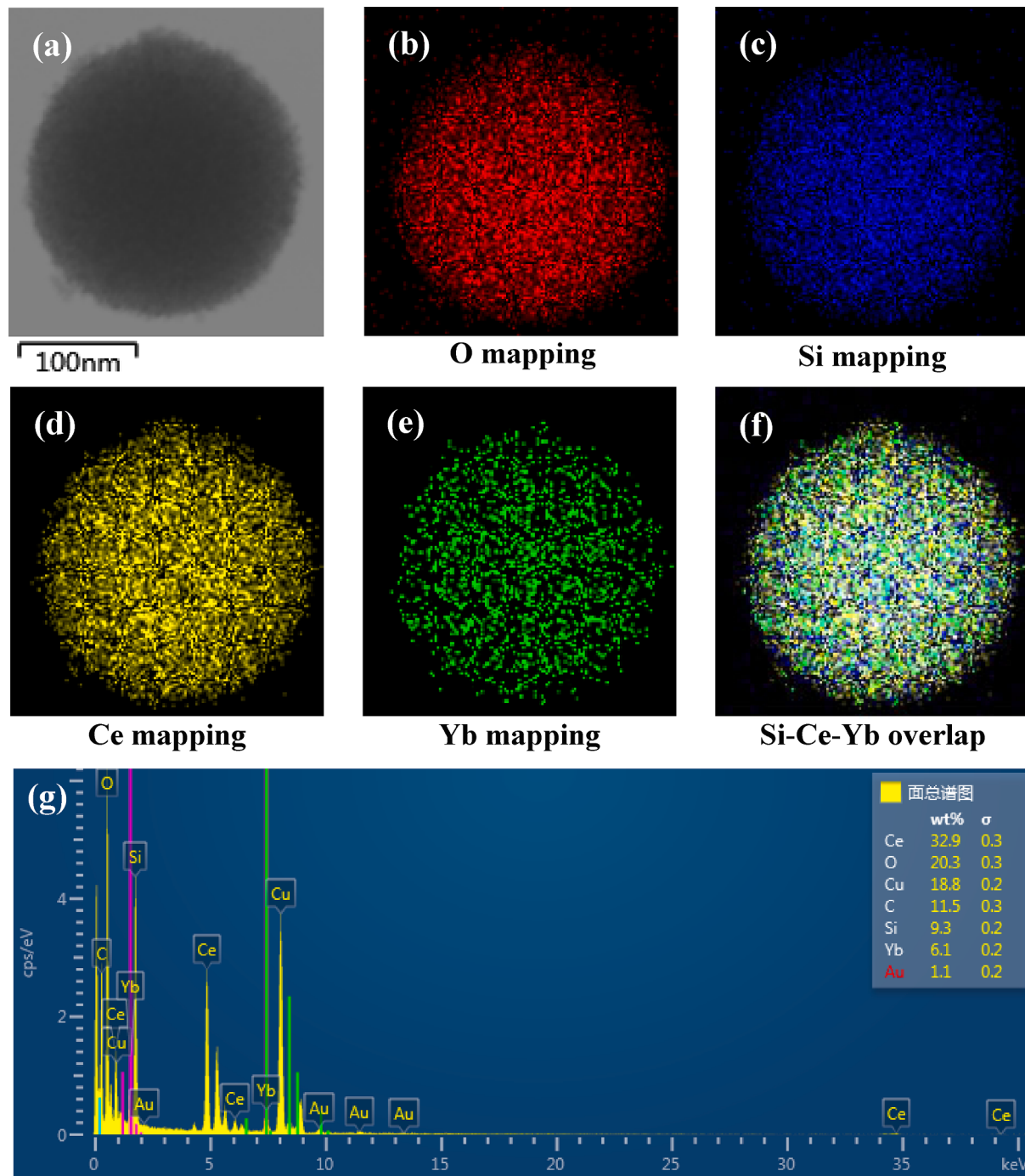


Fig. 5. HAADF-STEM image (a) and STEM-EDX elemental mapping of (b) O, (c) Si, (d) Ce, (e) Yb elements, (f) Si-Ce-Yb overlap, (g) atomic content data of the individual mSiO₂/Yb-CeO₂.

La-CeO₂, and Yb-CeO₂ were also calculated to be ca. 3.09, 2.60, and 2.61 nm, respectively.

Fig. 7 shows the Raman spectra of pure, La- and Yb-doped composite samples recorded under ambient conditions with an excitation wavelength of 532 nm of the laser. One intense band at ca. 460 cm⁻¹ and a weak band at ca. 600 cm⁻¹ can be clearly observed. The high-intensity bands can be attributed to the Raman-active vibrational mode (F_{2g}) of fluorite-type structure, corresponding to the symmetrical stretching vibration of the oxygen atoms around cerium ions in CeO₂ units [37,38,40]. No signals related to La₂O₃ or Yb₂O₃ can be found in the Raman spectra of the doped samples, which are consistent with the XRD results (Fig. 6). For the doped samples, the slight shifting of F_{2g} peaks

over lower frequency bands also suggests the incorporation of La³⁺ or Yb³⁺ ions into CeO₂ lattices and the formation of Ce-La-O or Ce-Yb-O solid solutions. In addition, the weak Raman bands ranged from 510 to 680 cm⁻¹ can include the contributions of lattice VOs and reduced Ce³⁺ cations. Therein, the signal centered at ca. 560 cm⁻¹ can be ascribed to the extrinsic VOs produced to maintain the charge neutrality after substituting Ce⁴⁺ ions La³⁺ or Yb³⁺ ions. The band located at ca. 600 cm⁻¹ can be assigned to the intrinsic VOs originated from the presence of Ce³⁺ ions at CeO₂ surfaces. As proposed by Luo and coworkers [41,42], the former can be attributed to the different oxidation state of the dopant compared to that of Ce⁴⁺, while the latter can be due to the different ionic radius of the dopant compared to that of Ce⁴⁺. The VO

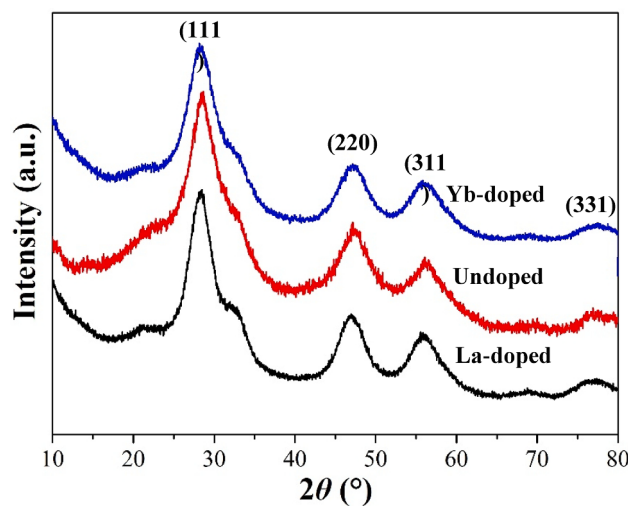


Fig. 6. XRD patterns of the pure, La- and Yb-doped mSiO₂/CeO₂ samples.

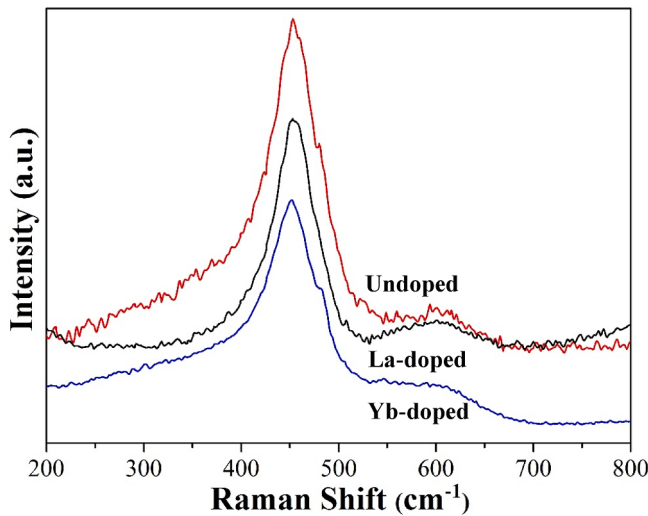


Fig. 7. Raman spectra of pure, La- and Yb-doped mSiO₂/CeO₂ samples.

and Ce³⁺ concentrations can be also evaluated by the intensity ratio of ca. 600 cm⁻¹ band to ca. 460 cm⁻¹ peak. As expected, intensity ratio data of La-doped (0.21) and Yb-doped samples (0.17) are higher than that of pure CeO₂ (0.14), suggesting the enrichments of VOs and Ce³⁺ ions in mSiO₂/La-CeO₂ and mSiO₂/Yb-CeO₂ composites. Consequently, the partial substitution will contribute to the generation of structure defects due to charge compensation and lattice distortion in CeO₂ materials [33]. It is commonly recognized that Ce³⁺ concentration can be correlated to the VOs at CeO₂ surfaces, which are created when Ce⁴⁺ ions are transformed to Ce³⁺ ions, thus leading to the formation of VOs [36,43]. The produced Ce³⁺ ions at CeO₂ surfaces can be expected to enhance the tribocatalytic and photochemical activities of the proposed mSiO₂/La-CeO₂ and mSiO₂/Yb-CeO₂ abrasive systems in CMP and PCMP processes.

The oxidation state of the elements and surface composition of the pure, La- and Yb-doped mSiO₂/CeO₂ samples were further investigated by XPS technique. Fig. 8 presents the wide survey XPS spectra, high-resolution Ce 3d core level spectra and the corresponding peak fitting results. The XPS Ce 3d5/2 and 3d3/2 doublet peaks are usually denoted as u and v, respectively. The Ce 3d spectra can be deconvoluted into five pairs of the spin-orbital doublets (3d5/2 and 3d3/2): v₀/u₀; v/u; v'/u'; v''/u''; v'''/u''' [44,45]. Herein, v₀/u₀ and v'/u' correspond to Ce³⁺ 3d final

states, and v/u, v''/u'', and v'''/u''' refer to Ce⁴⁺ 3d final states. The amount of surface Ce³⁺ species can be semiquantitatively evaluated using the following equations (2)-(4):

$$A(\text{Ce}^{4+}) = A_v + A_{v''} + A_{v'''} + A_u + A_{u''} + A_{u'''} \quad (2)$$

$$A(\text{Ce}^{3+}) = A_{v0} + A_{u0} + A_{v'} + A_{u'} \quad (3)$$

$$\text{Ce}^{3+} (\%) = \frac{A(\text{Ce}^{3+})}{A(\text{Ce}^{3+}) + A(\text{Ce}^{4+})}$$

where A is the integrated area corresponding to peak v or u. The concentration of Ce³⁺ for the pure mSiO₂/CeO₂, mSiO₂/Yb-CeO₂, and mSiO₂/La-CeO₂ were determined to be 37.45 %, 40.58 %, and 44.02 %, respectively. The substitution of La³⁺ or Yb³⁺ ions with Ce⁴⁺ ions contribute to the formation of Ce³⁺ species, which also increases the VO concentration of CeO₂-based materials due to a charge compensation mechanism [36,43]. The XPS data are consistent with the Raman results (Fig. 7).

3.2. Polishing performance evaluations

Compared to available light or electron microscopes, AFM is the most versatile and powerful analytical technique operated in different modes (contact, tapping, etc.) and environments (air, solution, etc.) to microscopically characterize the topography with extremely high spatial resolution and accuracy (up to Angstrom scale). In this work, the surface characteristics and planarization performances of commercial CeO₂, non-porous sSiO₂/CeO₂, mSiO₂/La-CeO₂ and mSiO₂/Yb-CeO₂ abrasive particles were compared in terms of high-resolution AFM.

The surface morphologies of the fused silica substrates after CMP and/or PCMP with different abrasive types are compared in Fig. 9 with an AFM scale bar of ± 0.2 nm. After pre-CMP (rough polishing stage) with commercial CeO₂ abrasives, distinct rolling and/or sliding microscratches (Fig. 9a) were left on the substrate surface from mechanical friction and abrasion. And the maximum scratch depth was determined to be ~ 5 nm in terms of cross-section analyses. In addition, many residual abrasive particles (bright spots) can be clearly observed from the presented AFM height image. It is commonly recognized that the residual products can be responsible for an enlarged surface roughness (3.38 Å of R_a, 5.55 Å of R_q, 6.65 Å of R_z). Fig. 9b shows an improved surface quality of the quartz glass after CMP with non-porous sSiO₂/CeO₂ particles, although there are still some shallow scratches on the finished surface. And the average R_a, R_q, and R_z roughness decreased to 2.72 Å, 3.92 Å, and 3.51 Å, respectively. In this work, the developed mSiO₂/La-CeO₂ (Fig. 9c and d) and mSiO₂/Yb-CeO₂ (Fig. 9e and f) abrasives offered ultra-smooth and scratch-free surfaces with angstrom-level accuracy under both conventional CMP and ultraviolet irradiation-assisted PCMP conditions. The detailed roughness and SAD data are summarized in Tables 1 and 2. As shown, the R_a, R_q, and R_z roughness achieved by La- and Yb-doped composite particles are much lower than those of commercial CeO₂ and rigid sSiO₂/CeO₂ abrasives.

The maximum asperity height, the maximum valley depth, and PV data were determined by sectional line scan analyses along the white dotted lines in 2D-AFM images (Lines 1–6). By comparison with the pre-finished surface (Fig. 10a) and the surface after CMP with sSiO₂/CeO₂ (Fig. 10b), the proposed mSiO₂/La-CeO₂ (Fig. 10c and d) and mSiO₂/Yb-CeO₂ (Fig. 10e and f) achieved obviously reduced PV values and topographical variation levels. The corresponding oblique and lateral AFM views of the surfaces before and after polishing are also presented in Fig. 11. As verified by these topography results, the La- and Yb-doped composite abrasive systems contribute to producing atomically smooth quartz glass surfaces, thus achieving superior polishing performance in virtue of appropriate synergy of mechanical function and chemical function.

In order to evaluate the structural stability of the as-prepared abrasives, the mSiO₂/Yb-CeO₂ and mSiO₂/La-CeO₂ abrasives in the used

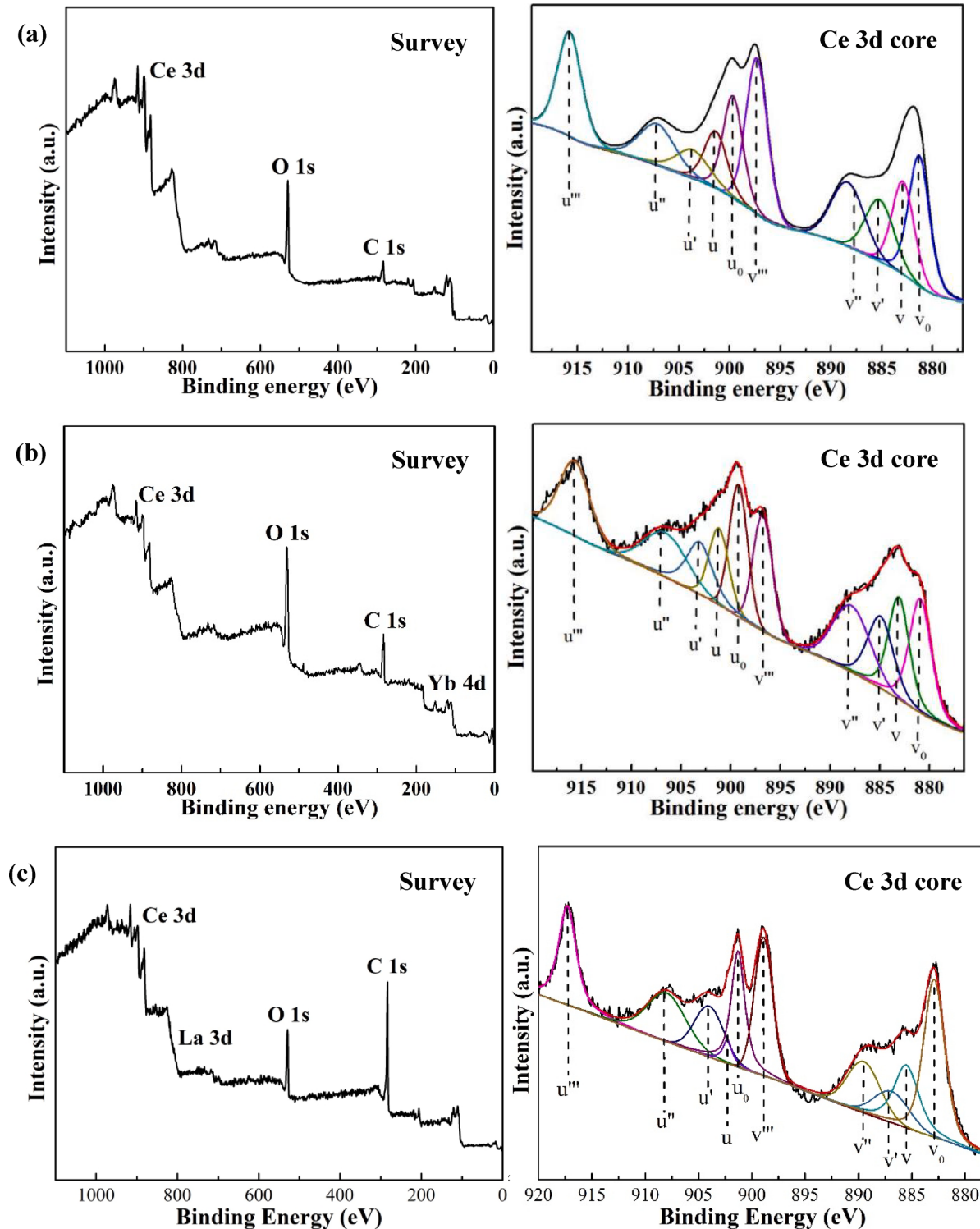


Fig. 8. XPS spectra of (a) mSiO₂/CeO₂, (b) mSiO₂/Yb-CeO₂, (c) mSiO₂/La-CeO₂ samples.

polishing slurries were examined by TEM observations. As shown in Fig. 12, no obvious changes in particle morphology and structure can be observed by comparison with the abrasives prior to use (Fig. 4), indicating that the developed abrasives present a satisfactory core–shell mechanical stability under an applied pressure and friction in the CMP processes. In addition, the quartz glass samples after polishing with mSiO₂/La-CeO₂ abrasives were examined by SEM observations. As expected, the polished sample presents a smooth mirror appearance, and the surface defects (residues, scratches, pits, cracks, etc.) can be hardly

found from Fig. 13.

During polishing with the mSiO₂-involved abrasives, the quartz glass surface interacted with the CeO₂ nanocrystals surrounding the low-modulus mSiO₂ spheres. Importantly, the larger mSiO₂ inner cores could act as an elastic carrier for the deposited CeO₂ and brings them in contact with the workpieces more gently and efficiently [16–21,26–28,46,47]. The presented data clearly demonstrate that mSiO₂ spheres as soft cores effect for the friction to substrates. The non-rigid mSiO₂/La-CeO₂ and mSiO₂/Yb-CeO₂ particles might elastically

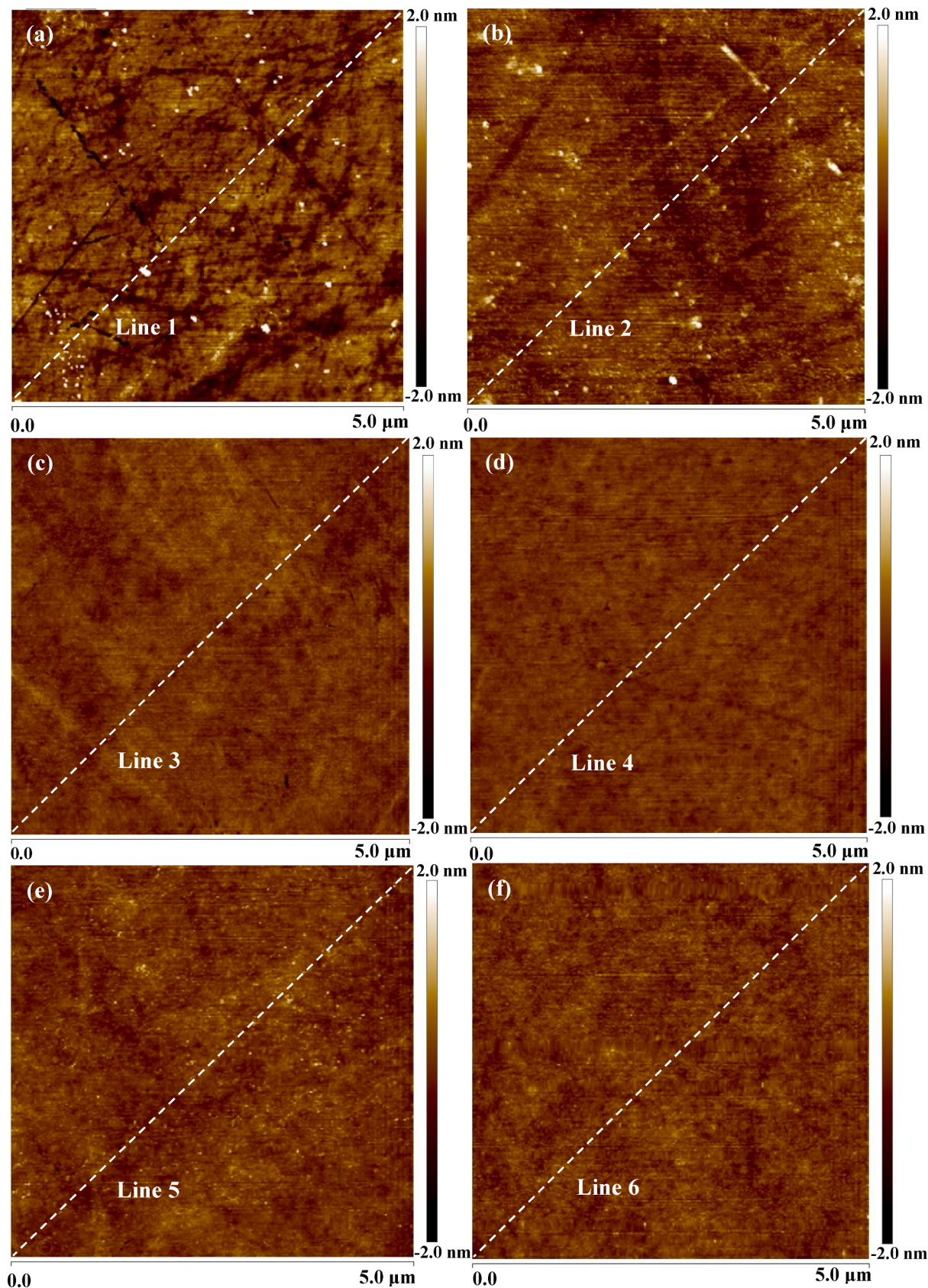


Fig. 9. AFM height images of the surfaces after finishing with (a) commercial CeO₂ (pre-finishing), (b) non-porous sSiO₂/CeO₂ (CMP), (c) mSiO₂/La-CeO₂ (CMP), (d) mSiO₂/La-CeO₂ (PCMP), (e) mSiO₂/Yb-CeO₂ (CMP), mSiO₂/Yb-CeO₂ (PCMP).

Table 1

Surface features of the quartz glasses after CMP and PCMP with mSiO₂/La-CeO₂ abrasive systems.

CMP	R _a (Å) ^a	R _q (Å) ^b	R _z (Å) ^c	Surface Area Difference (%) ^d
Run 1	1.54	1.98	2.26	0.00674
Run 2	1.56	1.98	2.09	0.00559
Run 3	1.53	2.02	2.31	0.00664
Average	1.54 ± 0.015	1.99 ± 0.023	2.22 ± 0.115	0.0063 ± 0.000638
PCMP	R _a (Å)	R _q (Å)	R _z (Å)	Surface Area Difference (%)
Run 1	1.31	1.65	1.94	0.00434
Run 2	1.20	1.53	1.86	0.00401
Run 3	1.45	1.87	2.20	0.00510
Average	1.32 ± 0.125	1.68 ± 0.172	2.00 ± 0.178	0.0045 ± 0.000559

^a Arithmetic average of the absolute values of the surface height deviations measured from the mean plane.

^b Root-mean-square average of height deviations taken from the mean image data plane.

^c Average difference in height between the highest peaks and valleys relative to the mean plane.

^d Difference between the image's 2D surface area and 3D projected surface area.

Table 2

Surface features of the quartz glasses after CMP and PCMP with mSiO₂/Yb-CeO₂ abrasive systems.

CMP	R _a (Å) ^a	R _q (Å) ^b	R _z (Å) ^c	Surface Area Difference (%) ^d
Run 1	1.70	2.17	2.98	0.0100
Run 2	1.74	2.25	3.30	0.0112
Run 3	1.75	2.29	3.42	0.0115
Average	1.73 ± 0.026	2.24 ± 0.061	3.23 ± 0.227	0.0109 ± 0.000794
PCMP	R _a (Å)	R _q (Å)	R _z (Å)	Surface Area Difference (%)
Run 1	1.72	2.22	3.32	0.00874
Run 2	1.48	1.93	2.80	0.00813
Run 3	1.59	2.15	3.11	0.00850
Average	1.60 ± 0.12	2.10 ± 0.15	3.08 ± 0.26	0.0085 ± 0.00031

deform under an applied down force, thus increasing the true contact area and decreasing the contact stress between abrasive particle and substrate surface [47]. Consequently, the non-rigid mSiO₂/La-CeO₂ and mSiO₂/Yb-CeO₂ abrasives offer damage-free and scratch-free surfaces by soft polishing/abrasion.

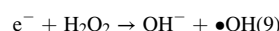
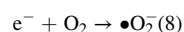
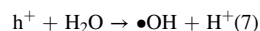
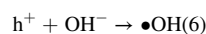
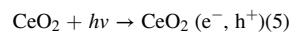
The zeta potential is a crucial factor for the dispersion stability of abrasive particles in polishing slurries. The larger absolute value of zeta potential commonly suggests that the particle dispersion is more stable in suspensions, resulting from the well-known electrostatic repulsion mechanism [18,48,49]. In this work, the Zeta potential values of the mSiO₂/Yb-CeO₂ and mSiO₂/La-CeO₂ slurries were determined to be -38.2 mV and -43.0 mV, respectively. As confirmed by Kelvin probe force microscopy, Kim and coworkers [50] proposed that the formation of VOs and the reduction of Ce⁴⁺ to Ce³⁺ increased the electron density of the trivalent lanthanide doped CeO₂ particles, thereby increasing the Fermi level of CeO₂. Moreover, the particles can be regarded as strongly cationic or anionic when the absolute value of the zeta potential is more than 30 mV [49]. As a consequence, the negatively charged mSiO₂/Yb-CeO₂ (-38.2 mV) and mSiO₂/La-CeO₂ (-43.0 mV) particles exhibited an acceptable dispersion stability in polishing slurries, which also contributed to the improved surface quality.

The removal efficiency data of commercial CeO₂ abrasives, La- and Yb-doped composites toward fused silica materials are provided in Fig. 14. The mSiO₂/La-CeO₂ and mSiO₂/Yb-CeO₂ abrasives involved

slurries offer significant RRs increases in comparison with the original CeO₂-based slurry. In addition, the introduction of ultraviolet irradiation during PCMP processes contributes to further RR enhancements. Compared to conventional CeO₂ abrasives, the overall RRs (CMP) of the mSiO₂/La-CeO₂ and mSiO₂/Yb-CeO₂ are increased by 175 %–335 %, from ca. 23.5 nm/min to ca. 64.6–102.2 nm/min. The RRs (PCMP) of the La- and Yb-doped composites are further enhanced by 54 %–89 % (ca. 121.8–157.4 nm/min).

The material removal process in CMP is based on chemical wear, i.e., a wear process dominated by chemical reaction, rather than abrasive wear. For glass polishing with CeO₂, it is commonly recognized that the multiple-step removal process involves chemical corrosion modification and tribocatalytic solid-state reaction (typically “chemical tooth” mechanism proposed by Cook [51]). Regarding to this model, water molecules enter the silica glass and break the composed Si–O bonds, thereby giving Si–OH (Si–O bonds fully hydrated Si(OH)₄) [52–55]. Consequently, water plays an extremely crucial role in weakening and softening Si–O bonds. This process can be further accelerated by compressive stress imposed into the surface by the abrasive particles [52]. It was further proposed that the presence of aqueous H₂O₂ contributed to enhancing the hydroxylation degree of quartz surfaces and improving the formation of Si–OH bonds. As revealed by nano-indentation tests [55], the hardness and elasticity modulus of quartz glass (6.58 GPa and 68.06 GPa) modified by 5 % H₂O₂ solution decreased by 12.7 % and 17.6 % by comparison with the original workpiece (7.54 GPa and 82.55 GPa). When CeO₂ particles contacted with quartz glass surfaces, the hydroxyl groups at CeO₂ surfaces reacted with silanol groups at modified quartz surfaces, thus forming Ce(III)–O–Si bonds with the assistance of water molecules [51,54]. The bonding between CeO₂ and SiO₂ enhanced the shearing force of particle abrasives, hence increasing the probability of material removal within a given indentation volume. Consequently, CeO₂ can enhance the material removal over SiO₂ by tribocatalytically reacting and bonding with SiO₂.

For CeO₂ semiconductor materials, when the energy of ultraviolet irradiation exceeds or equals to the band gap of CeO₂, the electrons can be excited from the O_{2p} valence band (VB) to an empty Ce_{4f} conduction band (CB), and the holes generate in the VB, thus forming electron–hole pairs [56,57]. The photogenerated electrons are localized on cerium ions, whereas holes are trapped on oxygen ions. The holes can react with OH[–] or H₂O forming hydroxyl radicals (•OH). The photogenerated electrons can also interact with surrounding O₂ and H₂O₂ (electron acceptors) to generate superoxide radicals (•O₂[–]) and •OH radicals. Overall, reactive oxygen species mainly resulted from an incomplete reduction reaction between light-excited electrons/holes and oxygen or water during the photocatalytic reaction process. These processes can be described as the following equations (5)–(9):



Furthermore, the photoexcited electrons may also transfer to the anti-bonding orbital of Si–O at the glass surfaces during ultraviolet irradiation-assisted PCMP. The charged electrons in the orbitals can be expected to extend the Si–O bonding distance [58], thus weakening the bonds and softening the fused glass surfaces.

The formation of Si(OH)₄ hydration layer on quartz surface highly affects the final RRs and surface quality in glass polishing [59–61]. In this work, the polishing slurries were adjusted to pH 8.0–8.5 range. In weakly alkaline conditions, the SiO₂ materials firstly reacted with OH[–] in aqueous solutions, as shown in equation (10), thereby leading to the formations of Si–OH bonds and Si(OH)₄ hydration layers.

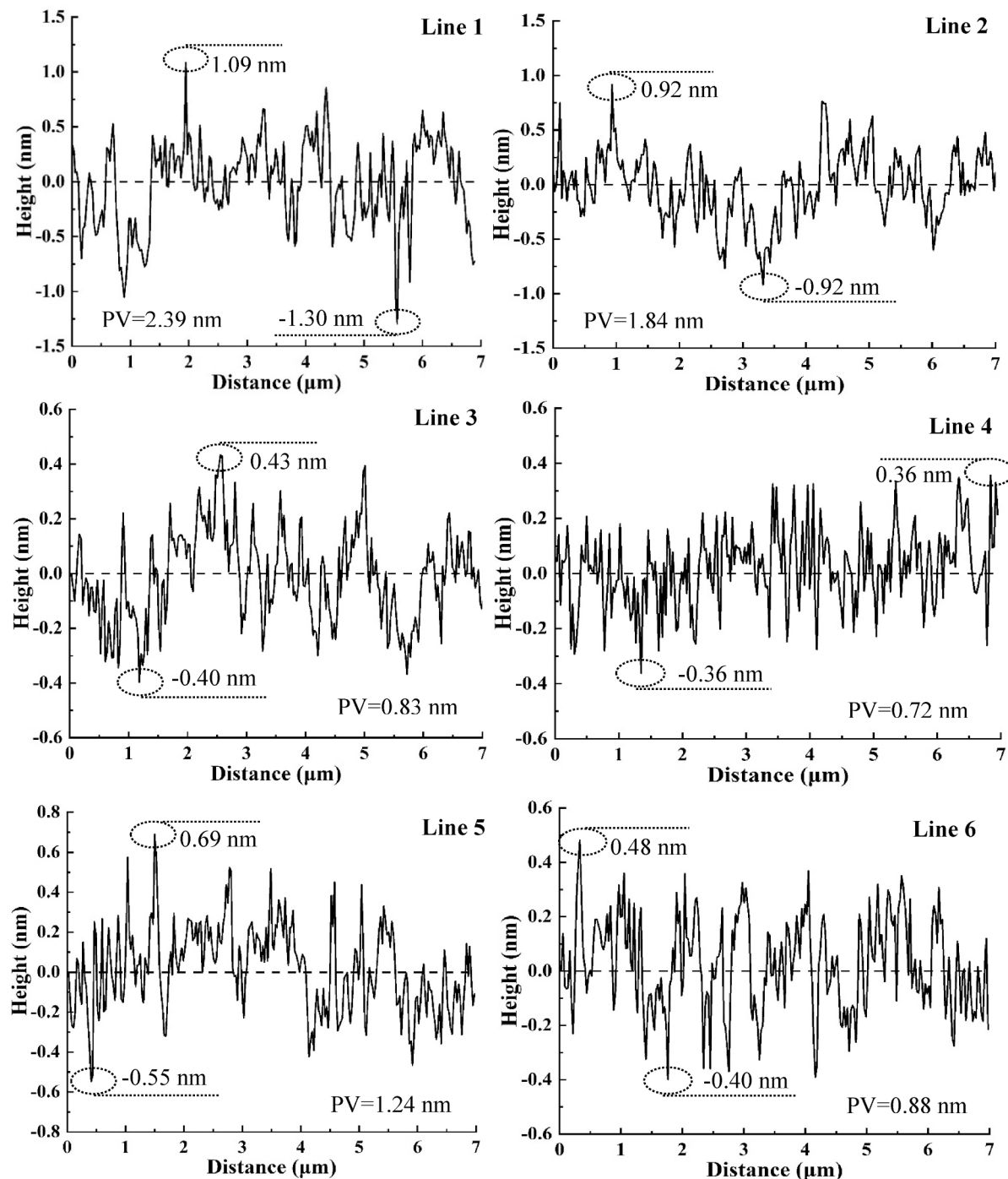
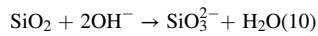


Fig. 10. The corresponding line-scan trace curves of (a) Line 1, (b) Line 2, (c) Line 3, (d) Line 4, (e) Line 5, (f) Line 6.



During ultraviolet irradiation-assisted PCMP, the photoinduced electrons can react with H_2O_2 generating $\bullet\text{OH}$ radicals, and the holes can also react with OH^- and H_2O producing $\bullet\text{OH}$ radicals. As proposed by Zhang and coworkers [24,25], the reactive oxygen species (typically $\bullet\text{OH}$ radicals) can be expected to accelerate the Si–O–Si bond breaking and the Si–OH bond creating as well as the $\text{Si}(\text{OH})_4$ production formation. Nevertheless, the chemical reactions involved in the free radicals-assisted SiO_2 surface modification should be further investigated in terms of *in situ* XPS, *in situ* Raman, *in situ* Fourier-transformed infrared spectroscope, electron spin resonance, electron paramagnetic

resonance, free radicals trapping, etc.

Consequently, the PCMP slurries exhibit stronger oxidation activity than CMP slurries, thus allowing an enhanced removal rate toward fused silica materials. It is commonly accepted that the enhanced separation efficiency of photogenerated electrons and holes ultimately leads to higher photocatalytic activity. For CeO_2 -based photocatalysts, the separation of electron–hole pairs is highly related to the amount of surface defects (typically VOs). The surface defects can act as charge carrier traps and adsorption sites where the charge transfer to adsorbed species, thus preventing the electron–hole recombination. In this work, the number of VO increases after introducing trivalent La^{3+} and Yb^{3+} ions with relatively low doping levels (~15 %) in CeO_2 lattices (as confirmed

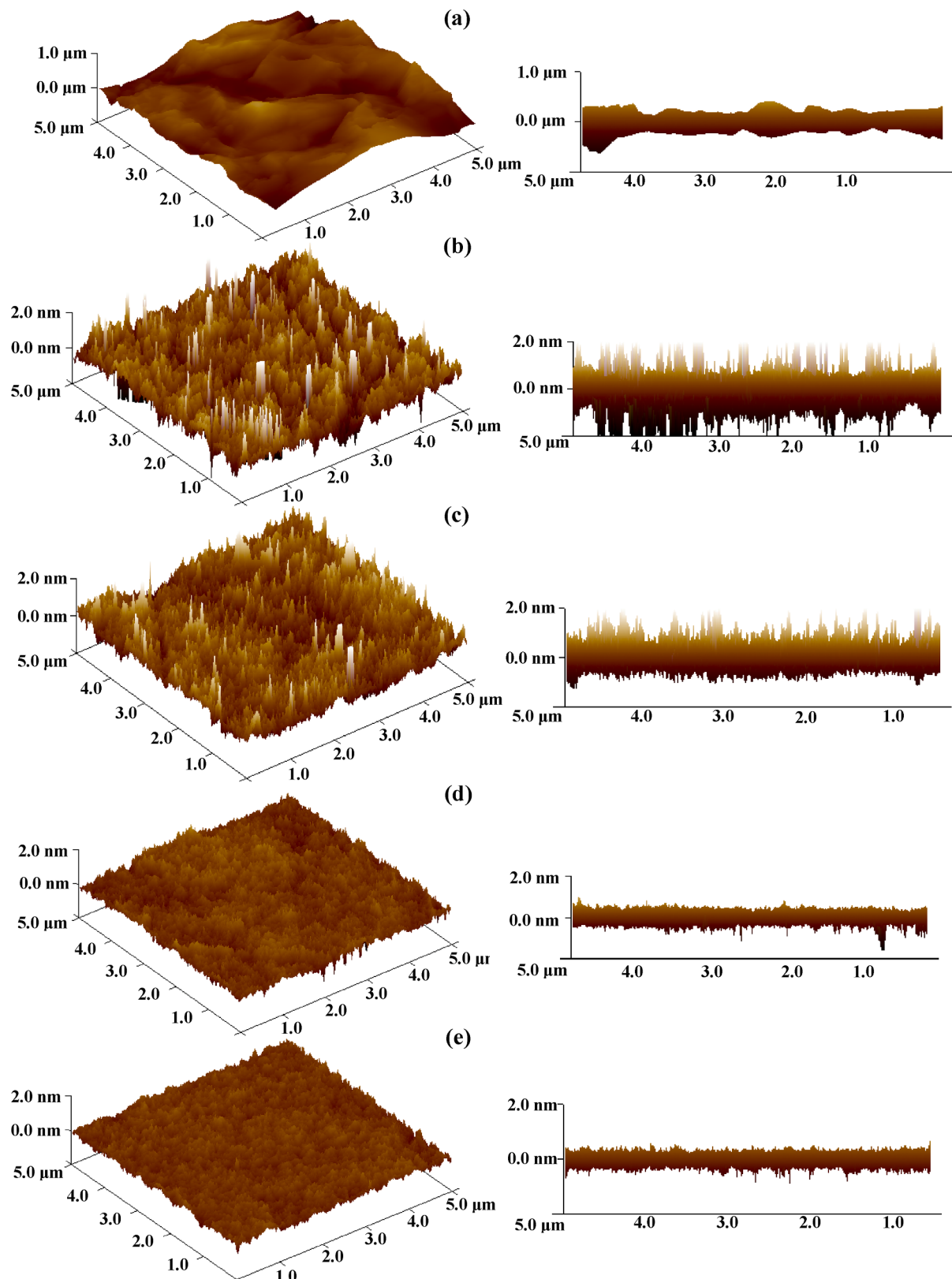


Fig. 11. The corresponding oblique and lateral AFM views driven from height images of the surfaces after finishing with (a) commercial CeO_2 (pre-finishing), (b) non-porous $\text{sSiO}_2/\text{CeO}_2$ (CMP), (c) $\text{mSiO}_2/\text{La-CeO}_2$ (CMP), (d) $\text{mSiO}_2/\text{La-CeO}_2$ (PCMP), (e) $\text{mSiO}_2/\text{Yb-CeO}_2$ (CMP), $\text{mSiO}_2/\text{Yb-CeO}_2$ (PCMP).

by Raman). The appropriate doping level and VO defect amount can be responsible for the photocatalytic activity improvement. It thereby contributes to the production efficiency of reactive oxygen species ($\bullet\text{OH}$,

$\bullet\text{O}_2^-$, etc.), and further accelerates the formation and removal of $\text{Si}(\text{OH})_4$ layer [9,24,25,62–64].

As verified by in-depth investigations [65–74], the Ce^{3+} species at

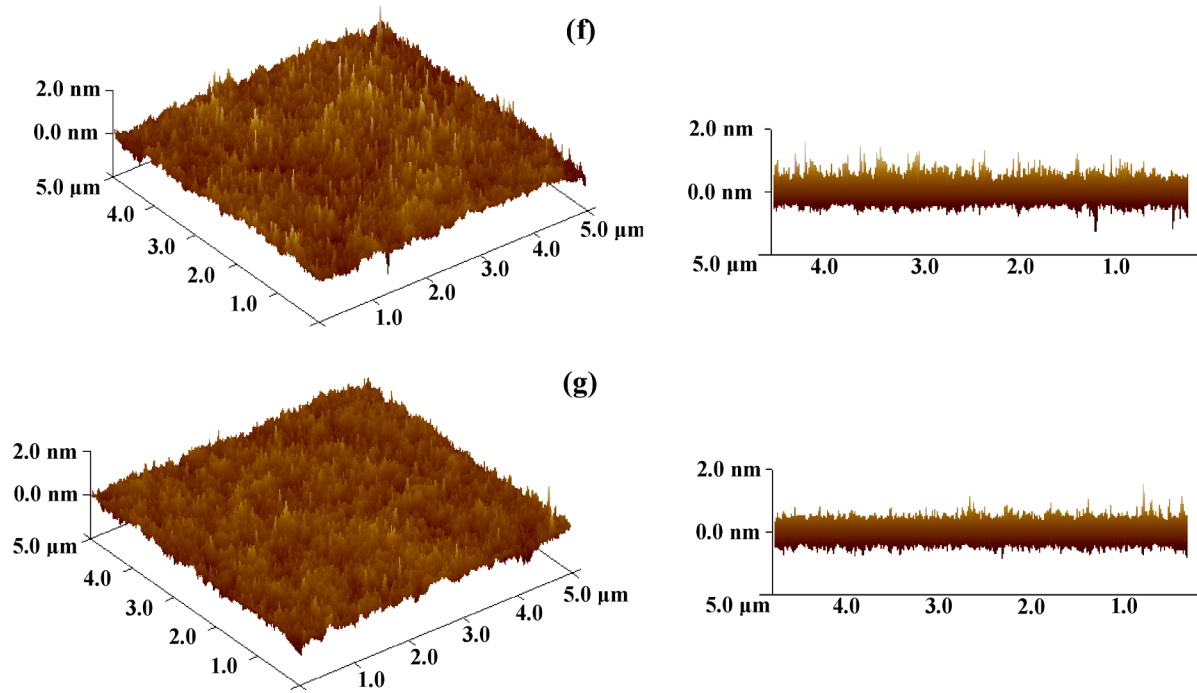
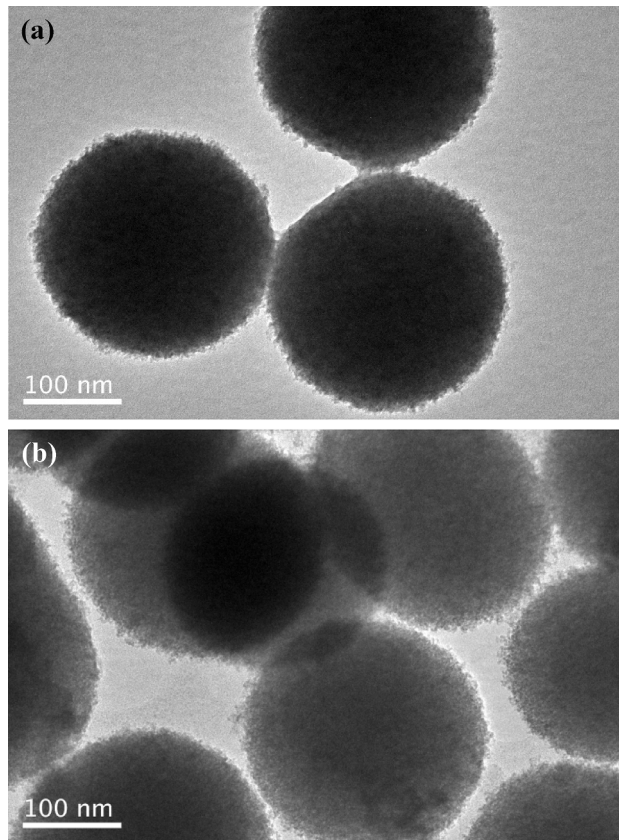
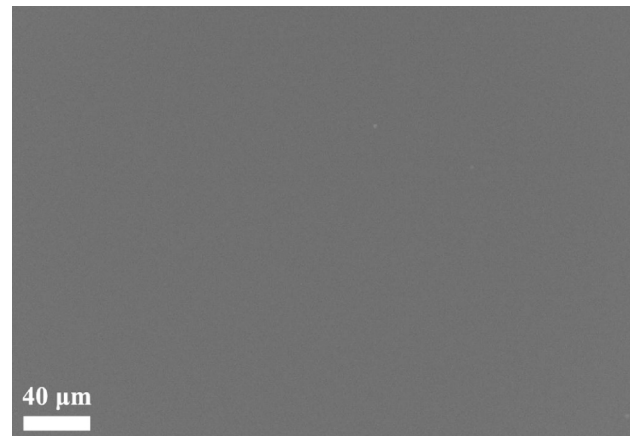


Fig. 11. (continued).

Fig. 12. TEM images of the (a) mSiO₂/La-CeO₂ and (b) mSiO₂/Yb-CeO₂ abrasive particles in the used polishing slurries.

CeO₂ abrasive surfaces, rather than Ce⁴⁺ species, can be expected to be reactive sites and accelerate the formation of Ce(III)-O-Si chemical bonds, thus enhancing the material removal toward SiO₂. It may be resulted from the enhanced adsorption affinity with SiO₂ surfaces and

Fig. 13. SEM image of the quartz glass sample after polishing with mSiO₂/La-CeO₂ abrasives.

the generated hydroxyl groups generated at CeO₂ surfaces by dissociation reaction of H₂O on Ce³⁺-involved defects. As confirmed by XPS, the Yb- and La-doped CeO₂ are rich in Ce³⁺ at the surfaces (40.58 % and 44.02 %) by comparison with the pure CeO₂ (37.45 %), while the enhanced chemical tooth property is favorable for the greater removal rates. It is also revealed that the concentration of Ce³⁺ ions is significantly involved in the RR improvement without deterioration of the surface quality for the developed abrasives. Compared to commercial CeO₂ abrasives, the proposed La- and Yb-doped mSiO₂/CeO₂ abrasive systems can achieve high removal rates while maintaining high-quality fused silica surfaces in both CMP and PCMP experiments.

4. Conclusions

In summary, we have successfully synthesized monodispersed La- and Yb-doped mSiO₂/CeO₂ composite particles as novel abrasive systems for improved polishing performance. The core/shell structures of the resulting products were verified by FESEM, HRTEM, and STEM-EDX

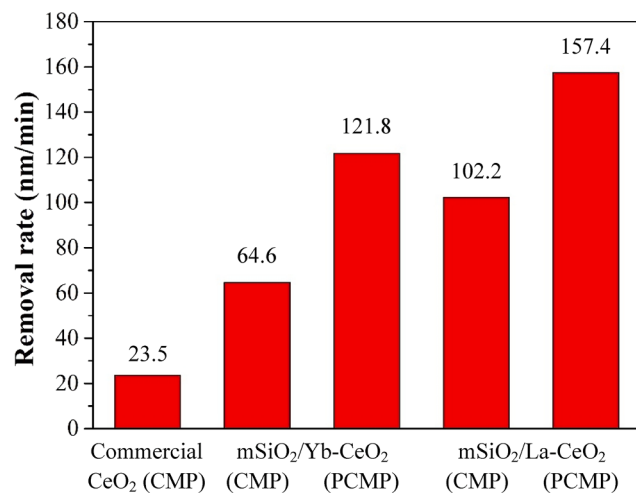


Fig. 14. Material removal rate data achieved with different abrasives under CMP and PCMP experimental conditions.

elemental mapping. Incorporation of slightly larger La³⁺ or Yb³⁺ ions in the CeO₂ lattices do not influence the structural nature, but increase the lattice parameter of CeO₂, as identified by XRD. Raman and XPS results revealed that more oxygen vacancies and Ce³⁺ species were created in La- and Yb-doped CeO₂ nanocrystals compared with those of pure CeO₂, thus leading to the improvements of photochemical and tribochemical activities. Polishing results confirmed that the mSiO₂/La-CeO₂ and mSiO₂/Yb-CeO₂ abrasive systems allowed soft polishing/abrasion and enabled high-quality surfaces without dishing, scratch, erosion, and residue defects, while maintaining high removal rates over quartz glasses. In addition, ultraviolet irradiation and soft abrasive polishing were simultaneously conducted as a result high-quality and high-efficiency PCMP was achieved. The presented data clearly demonstrate that a suitable design and precise control of the configuration and composition of CeO₂-based abrasive systems can be an efficient way to achieve both further high removal rate and high surface quality during ultraviolet irradiation-assisted PCMP. Further work will be focused on the cooperative roles of chemical (or photochemical) and tribochemical reactions, as well as mechanical friction in ultra-precise polishing assisted by reactive oxygen species.

CRediT authorship contribution statement

Zihan Kou: Writing – original draft, Investigation, Formal analysis, Data curation. **Chao Wang:** Writing – review & editing, Validation, Methodology, Funding acquisition. **Wenjin Zhou:** Validation, Software, Investigation, Formal analysis, Data curation. **Ailian Chen:** Supervision, Resources, Project administration, Funding acquisition. **Yang Chen:** Writing – review & editing, Visualization, Validation, Data curation, Conceptualization.

Declaration of competing interest

The authors declare that they have no known competing financial interests or personal relationships that could have appeared to influence the work reported in this paper.

Data availability

Data will be made available on request.

Acknowledgements

The work was supported by the National Natural Science Foundation

of China (Grant Nos. 52275174, 52175444, and 51875052), and the Sichuan Science and Technology Program (2021JDJQ0014).

References

- [1] N. Suzuki, R. Yamaguchi, Y. Hashimoto, H. Yasuda, S. Yamaki, Y. Mochizuki, Process state estimation in chemical mechanical polishing (CMP) by inverse analysis of in-process data, CIRP Annals 71 (2022) 273–276.
- [2] W. Xie, Z. Zhang, L. Wang, X. Cui, S. Yu, H. Su, S. Wang, Chemical mechanical polishing of silicon wafers using developed uniformly dispersed colloidal silica in slurry, J. Manuf. Process 90 (2023) 196–203.
- [3] Y. Li, Z. Zhang, X. Deng, H. Zhou, Y. Gu, C. Shi, S. Liu, W. Wang, W. Zhang, Novel green chemical mechanical polishing for an aluminum alloy and mechanisms interpreted by molecular dynamics simulations and measurements, Surf. Interfaces 42 (2023) 103493.
- [4] X. Cui, Z. Zhang, J. Yang, Z. Ren, H. Zhou, C. Shi, F. Meng, J. Feng, S. Zhao, Chemical mechanical polishing for potassium dihydrogen phosphate using four kinds of green developed slurries, J. Manuf. Process 101 (2023) 1158–1166.
- [5] G. Li, C. Xiao, S. Zhang, S. Luo, Y. Chen, Y. Wu, Study of the humidity-controlled CeO₂ fixed-abrasive chemical mechanical polishing of a single crystal silicon wafer, Tribol. Int. 178 (2023) 108087.
- [6] J. Murata, K. Hayama, M. Takizawa, Environment-friendly electrochemical mechanical polishing using solid polymer electrolyte/CeO₂ composite pad for highly efficient finishing of 4H-SiC (0001) surface, Appl. Surf. Sci. 625 (2023) 157190.
- [7] M. Zhou, Y. Cheng, M. Zhong, W. Xu, Macro and micro-nano machining mechanism for ultrasonic vibration assisted chemical mechanical polishing of sapphire, Appl. Surf. Sci. 640 (2023) 158343.
- [8] F. Fang, N. Zhang, D. Guo, K. Ehrmann, B. Cheung, K. Liu, K. Yamamura, Towards atomic and close-to-atomic scale manufacturing, Int. J. Extrem. Manuf. 1 (2019) 012001.
- [9] L. Xu, K. Park, H. Lei, P. Liu, E. Kim, Y. Cho, T. Kim, C.D. Chen, Chemically-induced active micro-nano bubbles assisting chemical mechanical polishing: Modeling and experiments, Friction 11 (2023) 1624–1640.
- [10] M. Uneda, K. Fujii, Highly efficient chemical mechanical polishing method for SiC substrates using enhanced slurry containing bubbles of ozone gas, Precis. Eng. 64 (2020) 91–97.
- [11] C. Hsieh, C. Chang, Y. Hsiao, C.A. Chen, C. Tu, H. Kuo, Recent advances in silicon carbide chemical mechanical polishing technologies, Micromachines 13 (2022) 1752.
- [12] G. Ma, S. Li, F. Liu, C. Zhang, Z. Jia, X. Yin, A review on precision polishing technology of single-crystal SiC, Crystals 12 (2022) 101.
- [13] H. Lee, Tribological study on photocatalysis-assisted chemical mechanical polishing of SiC, Lubricants 11 (2023) 229.
- [14] X. Zhang, X. Guo, H. Wang, R. Kang, S. Gao, Insight into polishing slurry and material removal mechanism of photoassisted chemical mechanical polishing of YAG crystals, Langmuir 39 (2023) 13668–13677.
- [15] E. Kim, J. Hong, S. Hong, C. Kanade, H. Seok, H. Kim, T. Kim, Improvement of oxide removal rate in chemical mechanical polishing by forming oxygen vacancy in ceria abrasives via ultraviolet irradiation, Mater. Chem. Phys. 273 (2021) 124967.
- [16] B. Gao, W. Zhai, Q. Zhai, M. Zhang, Novel polystyrene/CeO₂-TiO₂ multicomponent core/shell abrasives for high-efficiency and high-quality photocatalytic-assisted chemical mechanical polishing of reaction-bonded silicon carbide, Appl. Surf. Sci. 484 (2019) 534–541.
- [17] A. Chen, T. Wang, Y. Chen, S. Wang, Y. Chen, Development of polystyrene/polyaniline/ceria (PS/PANI/CeO₂) multi-component abrasives for photochemical mechanical polishing/planarization applications, Appl. Surf. Sci. 575 (2022) 151784.
- [18] Y. Fan, J. Jiao, L. Zhao, J. Tang, Preparation of lanthanide-doped polystyrene/CeO₂ abrasives and investigation of slurry stability and photochemical mechanical polishing performance, Colloid Surf. A 656 (2023) 130508.
- [19] Y. Chen, L. Zhong, A. Chen, M. Fu, X. Lu, Highly dispersed Gd-CeO₂ nanocrystals supported on mesoporous silica composite particles towards photochemical (photo-assisted chemical) mechanical polishing, Ceram. Int. 49 (2023) 16932–16943.
- [20] M. Wang, Z. Mu, T. Wang, Y. Chen, A. Chen, Double-layered core-shell heterostructures of mSiO₂@CdS@CeO₂ abrasive systems toward photochemical mechanical polishing (PCMP) applications, Appl. Surf. Sci. 614 (2023) 156274.
- [21] T. Wang, Y. Chen, A. Chen, Y. Chen, Development of carbon sphere/ceria (CS/CeO₂) heterostructured particles and their applications to functional abrasives toward photochemical mechanical polishing, Appl. Surf. Sci. 593 (2022) 153449.
- [22] Q. Zhang, J. Pan, Z. Zhuo, M. Xiang, Q. Yan, Abrasion behavior of TiO₂ catalyzing H₂O₂ to synergistically remove single crystal 6H-SiC under ultraviolet irradiation, Surf. Interfaces 38 (2023) 102781.
- [23] W. Jiang, H. Zhou, Y. Yang, S. Hu, J. Song, J. Ji, J. Song, A synergistic polishing technology by mixed abrasives with photocatalysis and fenton reaction, Mat. Sci. Semicon. Proc. 166 (2023) 107734.
- [24] Y. Fan, Z. Zhang, J. Yu, X. Deng, C. Shi, H. Zhou, F. Meng, J. Feng, Atomic surface of quartz glass induced by photocatalytic green chemical mechanical polishing using the developed SiO₂@TiO₂ core-shell slurry, Nanoscale Adv. (2023), <https://doi.org/10.1039/d3na00991b>.
- [25] C. Shi, Y. Fan, Z. Zhang, X. Deng, J. Yu, H. Zhou, F. Meng, J. Feng, Development of core-shell SiO₂@A-TiO₂ abrasives and novel photocatalytic chemical machinal polishing for atomic surface of fused silica, Appl. Surf. Sci. 652 (2024) 159293.

- [26] Z. Li, L. Jin, Z. Cao, C. Zhang, X. Cao, G. Han, S. Peng, Y. Liu, Development and characterization of a novel RE₃₊ doped core-shell CeO₂ abrasive system and its glass CMP investigations, *Appl. Surf. Sci.* 638 (2023) 158055.
- [27] C. Zhou, X. Xu, L. Dai, H. Gong, S. Lin, Chemical-mechanical polishing performance of core-shell structured polystyrene@ceria/nanodiamond ternary abrasives on sapphire wafer, *Ceram. Int.* 47 (2021) 31691–31701.
- [28] J. Murata, K. Yodogawa, K. Ban, Polishing-pad-free electrochemical mechanical polishing of single-crystalline SiC surfaces using polyurethane-CeO₂ core-shell particles, *Int. J. Mach. Tool. Manu.* 114 (2017) 1–7.
- [29] L. Wang, G. Ren, W. Xie, J. Zhang, D. Pan, H. Su, S. Wang, Controllable synthesis of core-shell SiO₂@CeO₂ abrasives for chemical mechanical polishing on SiO₂ film, *Colloid Surf. A* 682 (2023) 132901.
- [30] J. Liu, Z. Zhang, C. Shi, Z. Ren, J. Feng, H. Zhou, Z. Liu, F. Meng, S. Zhao, Novel green chemical mechanical polishing of fused silica through designing synergistic CeO₂/h-BN abrasives with lubricity, *Appl. Surf. Sci.* 637 (2023) 157978.
- [31] R.G. Chaudhuri, S. Paria, Core/shell nanoparticles: Classes, properties, synthesis mechanisms, characterization, and applications, *Chem. Rev.* 112 (2012) 2373–2433.
- [32] G.A. Drake, L.P. Keating, M. Shim, Design principles of colloidal nanorod heterostructures, *Chem. Rev.* 123 (2023) 3761–3789.
- [33] J. Zheng, B. Fan, X. Chen, J. Qin, F. Wang, R. Wang, X. Deng, Liu, Rare-earth doping in nanostructured inorganic materials, *Chem. Rev.* 122 (2022) 5519–5603.
- [34] Y. Chen, Z. Li, J. Qin, A. Chen, Monodispersed mesoporous silica (mSiO₂) spheres as abrasives for improved chemical mechanical planarization performance, *J. Mater. Sci.* 51 (2016) 5811–5822.
- [35] J.G. Li, T. Ikegami, T. Mori, T. Wada, Reactive Ce_{0.8}RE_{0.2}O_{1.9} (RE = La, Nd, Sm, Gd, Dy, Y, Ho, Er, and Yb) powders via carbonate coprecipitation. 1. Synthesis and characterization, *Chem. Mater.* 13 (2001) 2913–2920.
- [36] A.D. Liyanage, S.D. Perera, K. Tan, Y. Chabal, K.J. Balkus Jr, Synthesis, characterization, and photocatalytic activity of Y-doped CeO₂ nanorods, *ACS Catal.* 4 (2014) 577–584.
- [37] S. Xue, Q. Li, L. Wang, W. You, J. Zhang, R. Che, Copper- and Cobalt-codoped CeO₂ nanospheres with abundant oxygen vacancies as highly efficient electrocatalysts for dual-mode electrochemical sensing of MicroRNA, *Anal. Chem.* 91 (2019) 2659–2666.
- [38] A. Singhania, High surface area M (M = La, Pr, Nd, and Pm)-doped ceria nanoparticles: Synthesis, characterization, and activity comparison for CO oxidation, *Ind. Eng. Chem. Res.* 56 (2017) 13594–13601.
- [39] E.Y. Pikalova, A.A. Murashkina, V.I. Maragou, A.K. Demin, V.N. Strekalovsky, P.E. Tsikarous, CeO₂ based materials doped with lanthanides for applications in intermediate temperature electrochemical devices, *International Journal of Hydrogen Energy* 36 (2011) 6175–6183.
- [40] C. Alvarez-Galvan, P.G. Lustemberg, F.E. Oropeza, B. Bachiller-Baeza, M.D. Ospina, M. Herranz, J. Cebollada, L. Collado, J.M. Campos-Martin, V.A. de la Peña-O'Shea, J.A. Alonso, M.V. Ganduglia-Pirovano, Highly active and stable Ni/La-doped ceria material for catalytic CO₂ reduction by reverse water-gas shift reaction, *ACS Appl. Mater. Interfaces* 14 (2022) 50739–50750.
- [41] M. Guo, J. Lu, Y. Wu, Y. Wang, M. Luo, UV and visible Raman studies of oxygen vacancies in rare-earth-doped ceria, *Langmuir* 27 (2011) 3872–3877.
- [42] L. Li, F. Chen, J. Lu, M. Luo, Study of defect sites in Ce_{1-x}MxO_{2-δ} (x = 0.2) solid solutions using Raman spectroscopy, *J. Phys. Chem. A* 115 (2011) 7972–7977.
- [43] M.A. Mavuso, P.R. Makgwane, S.S. Ray, Heterostructured CeO₂–M (M = Co, Cu, Mn, Fe, Ni) oxide nanocatalysts for the visible-light photooxidation of pinene to aroma oxygenates, *ACS Omega* 5 (2020) 9775–9788.
- [44] S. Zhao, D. Kang, Y. Liu, Y. Wen, X. Xie, H. Yi, X. Tang, Spontaneous formation of asymmetric oxygen vacancies in transition-metal-doped CeO₂ nanorods with improved activity for carbonyl sulfide hydrolysis, *ACS Catal.* 10 (2020) 11739–11750.
- [45] K. Yan, C. Wen, R. Li, B. Zhang, T. Liu, Q. Liu, Z. Zhou, Morphological optimized CeO₂ and Cu-doped CeO₂ nanocrystals for hydrogen production by solar photo-thermochromic water splitting based on surface photoinduced oxygen vacancies, *Appl. Surf. Sci.* 636 (2023) 157779.
- [46] Q. Li, X. Li, Z. Ye, L. Wang, J. Pan, Y. Zhang, M. Ye, C. Wang, Effects of nanoscale abrasive agglomeration on material removal in magnetorheological finishing, *J. Am. Ceram. Soc.* 105 (2022) 2489–2499.
- [47] J. Chen, L. Fang, H. Chen, K. Sun, S. Dang, J. Han, Soft abrasive facilitating materials removal of SiO₂/Si bilayer materials: A molecular dynamics study, *Mater. Chem. Phys.* 293 (2023) 126927.
- [48] J. Cheng, S. Huang, Y. Li, T. Wang, L. Xie, X. Lu, RE (La, Nd and Yb) doped CeO₂ abrasive particles for chemical mechanical polishing of dielectric materials: Experimental and computational analysis, *Appl. Surf. Sc.* 506 (2020) 144668.
- [49] J. Cheng, S. Huang, X. Lu, Preparation of surface modified ceria nanoparticles as abrasives for the application of chemical mechanical polishing (CMP), *ECS J. Solid State Sci. Technol.* 9 (2020) 024015.
- [50] E. Kim, J. Lee, C. Bae, H. Seok, H. Kim, T. Kim, Effects of trivalent lanthanide (La and Nd) doped ceria abrasives on chemical mechanical polishing, *Powder Technol.* 397 (2022) 117025.
- [51] L.M. Cook, Chemical processes in glass polishing, *J. Non-Cryst. Solid* 120 (1990) 152–171.
- [52] X. Guo, S. Yuan, J. Huang, C. Chen, R. Kang, Z. Jin, D. Guo, Effects of pressure and slurry on removal mechanism during the chemical mechanical polishing of quartz glass using ReaxFF MD, *Appl. Surf. Sci.* 505 (2020) 144610.
- [53] W. Liu, S. Yuan, X. Guo, Atomic understanding of the densification removal mechanism during chemical mechanical polishing of fused glass, *Appl. Surf. Sci.* 591 (2022) 153166.
- [54] L. Brugnoli, K. Miyatani, M. Akaji, S. Urata, A. Pedone, New atomistic insights on the chemical mechanical polishing of silica glass with ceria nanoparticles, *Langmuir* 39 (2023) 5527–5541.
- [55] X. Guo, J. Huang, S. Yuan, C. Chen, Z. Jin, R. Kang, D. Guo, Effect of surface hydroxylation on ultra-precision machining of quartz glass, *Appl. Surf. Sci.* 501 (2020) 144170.
- [56] T. Montini, M. Melchionna, M. Monai, P. Fornasiero, Fundamentals and catalytic applications of CeO₂-based materials, *Chem. Rev.* 116 (2016) 5987–6041.
- [57] X. Huang, K. Zhang, B. Peng, G. Wang, M. Muhler, F. Wang, Ceria-based materials for thermocatalytic and photocatalytic organic synthesis, *ACS Catal.* 11 (2021) 9618–9678.
- [58] Y. Kakinuma, Y. Konuma, M. Fukuta, K. Tanaka, Ultra-precision grinding of optical glass lenses with La-doped CeO₂ slurry, *CIRP Ann. – Manuf. Techn.* 68 (2019) 345–348.
- [59] G. Xu, Z. Zhang, F. Meng, L. Liu, D. Liu, C. Shi, X. Cui, J. Wang, W. Wen, Atomic-scale surface of fused silica induced by chemical mechanical polishing with controlled size spherical ceria abrasives, *J. Manuf. Process* 85 (2023) 783–792.
- [60] Z. Tan, X. Jiang, Y. Mao, X. Long, H. Luo, Ultra-smooth surface with 0.4 Å roughness on fused silica, *Ceram. Int.* 49 (2023) 7245–7251.
- [61] L. Liu, Z. Zhang, C. Shi, H. Zhou, D. Liu, Y. Li, G. Xu, J. Feng, F. Meng, Atomic surface of fused silica and polishing mechanism interpreted by molecular dynamics and density functional theory, *Mater. Today Sustain.* 23 (2023) 100457.
- [62] X. Shi, C. Zou, G. Pan, H. Gong, L. Xu, Y. Zhou, Atomically smooth gallium nitride surface prepared by chemical mechanical polishing with S2O82-–Fe2+ based slurry, *Tribol. Int.* 110 (2017) 441–450.
- [63] K. Kawaguchi, Y. Wang, J. Xu, Y. Ootani, Y. Higuchi, N. Ozawa, M. Kubo, Cooperative roles of chemical reactions and mechanical friction in chemical mechanical polishing of gallium nitride assisted by OH radicals: tight-binding quantum chemical molecular dynamics simulations, *Phys. Chem. Chem. Phys.* 23 (2021) 4075–4084.
- [64] K. Kawaguchi, Y. Wang, J. Xu, Y. Ootani, Y. Higuchi, N. Ozawa, M. Kubo, Atom-by-atom and sheet-by-sheet chemical mechanical polishing of diamond assisted by OH radicals: A tight-binding quantum chemical molecular dynamics simulation study, *ACS Appl. Mater. Interfaces* 13 (2021) 41231–41237.
- [65] P.R.D. Veera, S. Peddeti, S.V. Babu, Selective chemical mechanical polishing of silicon dioxide over silicon nitride for shallow trench isolation using ceria slurries, *J. Electrochem. Soc.* 156 (2009) H936–H943.
- [66] P.R.V. Dandu, B.C. Peethala, S.V. Babu, Role of different additives on silicon dioxide film removal rate during chemical mechanical polishing using ceria-based dispersions, *J. Electrochem. Soc.* 157 (2010) H869–H874.
- [67] R. Srinivasan, P.V.R. Dandu, S.V. Babu, Shallow trench isolation chemical mechanical planarization: A Review, *ECS J. Solid State Sci. Technol.* 4 (2015) P5029–P5039.
- [68] C.M. Netzband, K. Dunn, Investigation into the effect of CMP slurry chemicals on ceria abrasive oxidation state using XPS, *ECS J. Solid State Sci. Technol.* 8 (2019) P629–P633.
- [69] C.M. Netzband, K. Dunn, Controlling the cerium oxidation state during silicon oxide CMP to improve material removal rate and roughness, *ECS J. Solid State Sci. Technol.* 9 (2020) 044001.
- [70] J. Ma, N. Xu, J. Hu, Y. Luo, Y. Lin, Y. Pu, Doping strategy on properties and chemical mechanical polishing performance of CeO₂ Abrasives: A DFT assisted experimental study, *Appl. Surf. Sci.* 623 (2023) 156997.
- [71] J. Ma, N. Xu, Y. Luo, Y. Lin, Y. Pu, Enhancing the Polishing Efficiency of CeO₂ Abrasives on the SiO₂ substrates by improving the Ce³⁺ concentration on their surface, *ACS Appl. Electron. Mater.* 5 (2023) 526–536.
- [72] J. Lee, E. Kim, C. Bae, H. Seok, J. Cho, K. Aydin, T. Kim, Improvement of oxide chemical mechanical polishing performance by increasing Ce³⁺/Ce⁴⁺ ratio in ceria slurry via hydrogen reduction, *Mat. Sci. Semicon. Proc.* 159 (2023) 107349.
- [73] X. Han, R. Liu, B. Tan, F. Wang, M. Yan, X. Zhao, J. Zhao, Research progress on the application of ceria nanoparticles as abrasives in dielectric layer CMP and post cleaning: Structure, morphology, doping, and mechanism, *Colloid Surf. A* 679 (2023) 132551.
- [74] Y.S. Lin, K.S. Lin, W.C. Tsai, N.V. Mdlovu, C.Y. Tang, U.S. Jeng, Cetyltrimethylammonium bromide reformed ceria nanocomposites of chemical mechanical planarization for silica wafers, *J. Taiwan Inst. Chem. Eng.* 150 (2023) 105079.